Research Square

Preprints are preliminary reports that have not undergone peer review.
They should not be considered conclusive, used to inform clinical practice,
or referenced by the media as validated information.

The effect of frame roughness and geometry on an electrically rotating thin film

Majid Panahi
Institute for Advanced Studies in Basic Sciences
Mohammad Hadi Sadri
Institute for Advanced Studies in Basic Sciences
Negin Mohammadzadeh
Institute for Advanced Studies in Basic Sciences
Davood Hesari
Institute for Advanced Studies in Basic Sciences
Ali-Reza Moradi
moradika@iasbs.ac.ir

Institute for Advanced Studies in Basic Sciences

Article

Keywords:

Posted Date: October 8th, 2026

DOI: https://doi.org/10.21203/rs.3.rs-10996338/v1

License: This work is licensed under a Creative Commons Attribution 4.0 International License.
Read Full License

Additional Declarations: No competing interests reported.

The effect of frame roughness and geometry on an electrically rotating thin film

Majid Panahi[1], Mohammad Hadi Sadri[1], Negin Mohammadzadeh[1], Davood Hesari[1], and Ali-Reza Moradi[1,2,*]

[1]Department of Physics, Institute for Advanced Studies in Basic Sciences (IASBS), Zanjan 45137-66731, Iran
[2]School of Quantum Physics and Matter, Institute for Research in Fundamental Sciences (IPM), Tehran 19395-5531, Iran
[*]moradika@iasbs.ac.ir

ABSTRACT

Applying external crossed electric fields to a suspended liquid film induces rotational flow. In practice, the enclosing frame of the film has edge roughness and corner bluntness, particularly for rectangular frames. In this paper, we investigate the effects of frame shape, edge roughness, and corner sharpness on the rotational behavior of the film through experiments and simulations. By tracking a microscopic tracer embedded in the film, we show that the roughness and shape of the frame are initially sensed through the tracer's trajectory and velocity, respectively. A frame-shape-dependent transition from circular fluidic streamlines to boundary-shaped streamlines is also observed. Simulations reveal that for rectangular frames, the curvature of the corners relative to the frame size governs this transition. The observations are explained using a model of charge induction in ohmic liquids coupled with hydrodynamic interactions. These findings may inform the design and application of integrated fluidic circuits.

Introduction

The manipulation of fluid flow in confined geometries has become a critical focus in microfluidics and electrohydrodynamics due to its wide-ranging applications in integrated fluid circuits, lab-on-a-chip technologies, micro-electromechanical systems, drug delivery, and biomedical devices[1–4]. Thin liquid films, such as soap films, provide an ideal experimental platform for studying electrohydrodynamic effects, where the behavior of fluids is strongly influenced by external electric fields. Understanding how these fields interact with the film geometry is essential for optimizing devices that rely on controlled fluid motion at the microscale[5,6]. In recent years, the phenomenon of the induced rotation in thin suspended polar liquid films by external electric fields has garnered significant attention. A notable example is the so-called "liquid film motor", in which the application of an electric field perpendicular to the film, combined with a current flowing through a liquid film leads to a controlled rotational flow within the film[7–10]. The ability to manipulate the direction and speed of the rotation in these films offers valuable insights into the potential use of electrohydrodynamics for flow control in microfluidic systems. Several physical parameters can potentially affect the rotational behavior. The influence of the external electric field configuration and the strength of the current magnitude, the geometry of the frame enclosing the film, the surface tension and dielectric properties of the film, and film thickness on the flow characteristics has been already studied[11–14]. The results of these studies enable optimizing the film rotations, which in turn, possess the potential to significantly enhance the efficiency and precision of liquid film motors, making them more versatile for practical applications.

In most of the proposed theoretical investigations, the governing equations for the electrohydrodynamics of the electroconvection in suspended polar films are used to extract the induced free charges and the electric fields on the liquid[15–19]. Then, from them the forces that induce the rotation and the rotational behavior parameters are computed. According to these theories, the interaction between the electric current and the induced charges in the film leads to apply torques on the polar molecules and generates the observed rotational motion. A similar theory has been also used to explain the rotation of a liquid bulk with a free surface, in which, at the free surface on the top of the liquid no slip condition, and at the bottom of the bulk constant shear stress are considered[14].

In either the experimental results or the theoretical investigations, it is always considered that the enclosing frame of the liquid film has an infinite smoothness and sharpness in the corners (in the case of rectangular shape frames). Practically, however, fabrication of such a frame is impossible. In this paper, we address the issue of the frame shape, its roughness, and the sharpness of the corners of the rectangular frame on the rotational behavior of thin films. Geometry plays a vital role in shaping the distribution of electric fields and, consequently, the resultant flow patterns in liquid film motors[18]. To consider this concern,

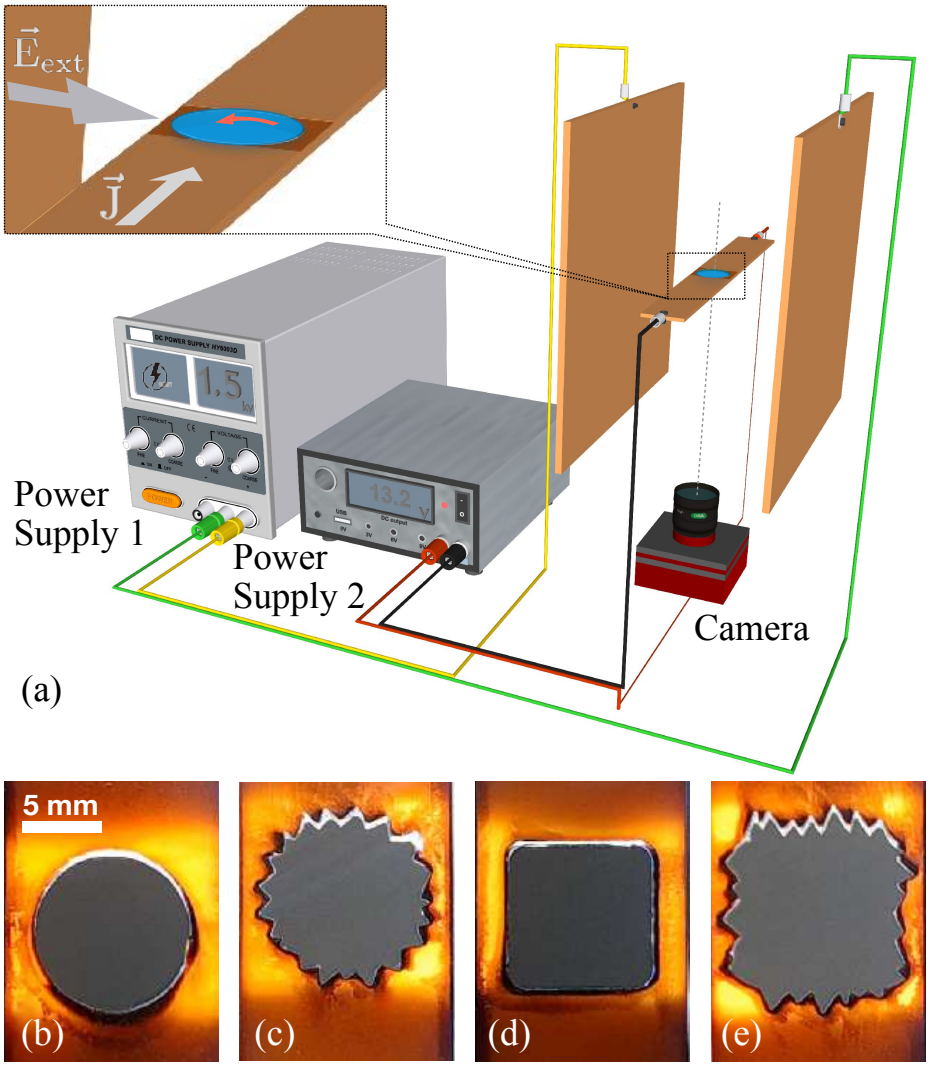


Figure 1. (a) Schematic of the experimental setup for studying electric-field-induced rotation in suspended liquid thin films. A soap film is formed across an aperture in an electrically insulating frame. Electrodes on opposite sides of the aperture are connected to a DC power supply (Power Supply 1, 30 V) to drive an in-plane current ($\vec{J}$), while a perpendicular electric field ($\vec{E}_{\text{ext}}$) is applied using parallel capacitor plates powered by a high-voltage source (Power Supply 2, 3.53 kV/cm). The inset shows a magnified view of the aperture, where the film is formed by sweeping a wet pad; rotation under crossed fields is recorded using a digital camera. (b)-(e) Images of four different frame geometries used in the experiments. In Supplementary Video 1, the videos of 10 s duration of a thin film suspended and rotating in circular, rough circular, square, and rough square frames are shown.

we examine the varied shapes of the supporting frame and apply controlled roughness on their edges and corner curvature of rectangular frames experimentally, and monitor the altering intensity of field distributions. Furthermore, in order to expand the influence of roughness and sharpness, we provide systematic simulation studies, and extract trajectories, velocity fields, and characteristic radius and velocity of rotation for each case.

The paper is organized as follows. In Section the experimental setup and data processing procedure are explained. In Section the theoretical description is presented, and in Section the simulation procedure is explained. The results are presented and discussed in Section , and the paper is concluded in Section .

Experimental procedure

Figure 1(a) illustrates the experimental arrangement devised to explore the crossed-electric field induced rotational behavior of suspended transparent liquid thin films. Also a magnified view of the film forming frame is shown in the inset. A soap

solution thin film is a common example to form a suspended, i.e., substrate-less thin film. Pure water does not provide optimal conditions, and to enhance the stability and responsiveness of the layer, we introduce a small amount of detergent to it. This allows for high sensitivity of the free layers and their movement upon applying even a very small external force. The liquid film is formed within a custom-designed electrically insulating frame that serves as both a boundary and a scaffold to support the film's fragile structure. The frame is built from FR-4 glass epoxy for its optimal balance of electrical insulation and moisture resistance; It has a relative permittivity of 4.4, which provides a stable platform for the application of electric fields, while its minimal water absorption rate (a mere 0.10% over 24 hours) ensures that external humidity does not compromise the integrity of the experiment. The electrodes on the opposite sides of the frame's aperture serve as conduits for the electric current and are connected to a DC voltage source (Power Supply 1, MPS-6005h, Matrix, 60V/5A), which is set to get 30 V. The wide connected area ensures a uniform current density across the film. This frame is connected to two electrodes and is placed between the parallel conductive plates of a large capacitor. The plates are powered by a high DC voltage source (Power Supply 2, PHYWE, HV-Power Supply, 0 to 10 kV DC), which can be finely tuned to create an external electric field (up to 3.53 kV/cm strength) perpendicular to the direction of the electric current in the liquid film. The liquid film is generated with precision by gently drawing a wet pad across the aperture of the frame which creates a uniform layer that spans the opening.

The liquid film rotates when the electric current flows through it and, simultaneously, the external electric field is applied in a perpendicular direction to the current flow. The rotational velocity depends on the applied external electric field and slightly on the flowing current. Videos of the rotating films under investigation are recorded using a digital camera (DCC1545M, Thorlabs, 8-bit dynamic range, and 5.2 μm pixel pitch) equipped with an imaging lens. This setup allows carefully studying the intricate interplay between applied electric fields and the hydrodynamics of thin liquid layers.

Particle-image velocimetry (PIV), which is a well-established technique in fluid mechanics[20,21], is employed to extract the velocity field of the fluid flow at numerous points simultaneously. For each experimental condition, a minimum of five videos are captured at a frame rate of 25 fps. Since the liquid films are transparent, tracer polystyrene particles with a diameter of 50 μm are introduced to visualize the flow, enabling the rotation characterization, i.e., determination of both the direction and velocity parameters. To investigate the influence of frame geometry and boundary conditions on the characteristics of the film motor, frames of various shapes are fabricated, including circular, rough circular, square, and rough square designs. In Figs. 1(b) to 1(e) pictures of the fabricated frames are shown. In Supplementary Video 1, the videos of 20 s duration of a thin film suspended and rotating in circular, rough circular, square, and rough square frames are shown.

Theory

According to the experimental conditions the physical thickness of the liquid film is much smaller than its diameter. Therefore, the rotating film may be treated as a 2D Newtonian fluid[15]. The physics of the phenomenon is described via the electroconvection theory, which provides the induced free charges and the electric fields on the liquid film under predefined experimental conditions. Then, we compute the acting forces and torques, and the rotational behavior parameters. The first governing equation for electrohydrodynamics of a thin liquid layer is the continuity equation or mass conservation of the Navier-Stokes equations:

$$\vec{\nabla}\cdot\vec{u}=0, \tag{1}$$

where $\vec{u}$ is the fluid velocity. Equation 1, gives the solenoidal velocity field as $\vec{u}=u_r\hat{r}+u_\theta\hat{\theta}$, considering the incompressibility condition. Also, the momentum conservation equation of the Navier-Stokes equations yields the flow velocity:

$$\rho\left[\frac{\partial\vec{u}}{\partial t}+(\vec{u}\cdot\vec{\nabla})\vec{u}\right]=-\vec{\nabla}P+\eta\vec{\nabla}^2\vec{u}+q\vec{E}, \tag{2}$$

in which the electric force, $q\vec{E}$, is also considered, q being the surface charge density. In Eq. 2, ρ is the film mass density, P is the pressure, and η is the viscosity. To preserve the conservation of charge, we need to include an ohmic conductive current density, $\sigma\vec{E}$, as well as a convective current density, $q\vec{u}$:

$$\frac{\partial q}{\partial t}=-\vec{\nabla}\cdot(\sigma\vec{E}+q\vec{u}), \tag{3}$$

where σ is the ohmic conductivity. The electric field in the thin film may be presented via potential function, $\vec{E}=-\vec{\nabla}_2\psi_2$, where ψ_2 and $\vec{\nabla}_2$ denote the 2D electrical potential and 2D gradient, respectively. The surface charge density right above the surface ($z=0^+$) is, therefore, described via the first Maxwell equation as[22]:

$$q=-2\varepsilon_0\partial_z\psi_3\big|_{z=0^+}, \tag{4}$$

in which the factor 2 corresponds to the two free surfaces of the liquid film. There are no free charges outside of the film, hence:

$$\nabla_3^2\psi_3 = \nabla_2^2\psi_3 + \frac{\partial^2\psi_3}{\partial z^2} = 0, \tag{5}$$

where, similarly, the subscript 3 denotes 3D potential and gradient. Given the aforementioned conditions and the spatial continuity of potential, we have:

$$\psi_2 = \psi_3(z=0). \tag{6}$$

For the frames with rough edges, despite the smooth edge ones, the no-slip boundary condition at the edges, i.e., $u_r = u_\theta = 0$, can no longer be considered. Normally, since the film is conductive, the free charges are induced on its surfaces due to the applied external field, and $\vec{\nabla}\cdot(q\vec{u})$ causes the charges to move with the fluid and produce the convective current. However, the roughness at the edges of the frame will change the charge distribution on the film surface substantially. According to Eqs. 3-5, the roughness caused changes in the charge distribution will, in turn, alter the charge distribution all over the film. The charge distribution changes will accordingly impose modifications on the governing equations.

As an approximation, a relation between the surface charge density, the potential, and the radius of the film (R) for ideal geometry, i.e., smooth edges for the frames with no-slip boundary conditions, can be expressed as[23]:

$$\psi_2 = \frac{Rq}{\varepsilon_0}. \tag{7}$$

However, the roughness of the frame edges in our configuration invalidates the assumption of rigid-body behavior near the boundary. Experimental and theoretical studies show that the roughness induces complex flow patterns near the boundary, leading to effective slower tangential velocity and breaking of the classical no-slip condition[24]. To model this effect, we adopt a partial-slip boundary condition, characterized by an effective slip length λ that encapsulates the averaged hydrodynamic impact of the rough structures. The modified boundary condition becomes[24,25]:

$$u_\theta\big|_{r=R} = \lambda \left.\frac{\partial u_\theta}{\partial z}\right|_{z=0}, \tag{8}$$

where λ is the slip length and depends on the statistical roughness metrics of the frame edge, such as root mean square of height (R_a) and correlation length (ℓ_c). For statistically random rough surfaces the slip length is often negative, implying a net slowdown of the adjacent fluid layer and effectively replacing the no-slip plane with a stick-slip boundary located within the roughness layer[26].

In addition to the hydrodynamic effect, roughness alters the electrical boundary conditions. The protrusions concentrate the electric field, leading to enhanced surface charge density near the rough edges. This creates two competing mechanisms: (1) reduced fluid velocity due to negative hydrodynamic slip, and (2) enhanced electrostatic driving force due to electric field concentration concentrated charges at roughness peaks. To model these competing effects, we introduce two dimensionless functions that capture the qualitative behavior. The reduction in angular velocity due to slip at rough edges can be modeled through a dimensionless function f[27]:

$$\omega_{\text{eff}} = \omega\left[1 - f\left(\frac{|\lambda|}{R}\right)\right], \tag{9}$$

where $f(0) = 0$, and f increases with $|\lambda|/R$, quantifying the velocity reduction due to slip. When the slip due to the edge roughness is included, the velocity field deviates from pure rigid rotation near the edges. Therefore, to satisfy the no-slip condition at the physical boundary while accounting for the slip effect, the velocity profile is modified as:

$$u_\theta(r) = \omega_{\text{eff}} r\left[1 - \left(\frac{r}{R}\right)^n\right], \quad n \geq 1, \tag{10}$$

where the slip effect is incorporated in the effective angular velocity ω_{eff}, and the profile ensures $u_\theta(R) = 0$ boundary condition. The increase of surface charge due to electric field concentration at roughness peaks is modeled through an increasing function f'[22]:

$$q_{\text{eff}} = q\left[1 + f'\left(\frac{R_a}{\ell_c}\right)\right], \tag{11}$$

where $f'(0) = 0$, and f' increases with the ratio R_a/ℓ_c, representing the field enhancement due to roughness. For small R_a/ℓ_c, f' is approximately linear, while it may saturate for large values. Consequently, considering the above effects Eq. 7 is corrected as:

$$\psi_2 = \frac{Rq_{\text{eff}}}{\varepsilon_0} = \frac{Rq}{\varepsilon_0}\left[1 + f'\left(\frac{R_a}{\ell_c}\right)\right]. \tag{12}$$

These modifications yield a final revised dimensionless governing equation for the potential as:

$$\frac{1}{r'}\frac{\partial \psi'}{\partial r'} + \frac{\partial^2 \psi'}{\partial r'^2} + K_{\text{eff}}\frac{\partial \psi'}{\partial \theta} + \frac{1}{r'^2}\frac{\partial^2 \psi'}{\partial \theta^2} = -K_{\text{eff}} r' \sin\theta, \tag{13}$$

where $r' = r/R$, $\psi' = \psi_2/ER$, and the effective dimensionless parameter is:

$$K_{\text{eff}} = \frac{\omega_{\text{eff}}\varepsilon_0 R}{\sigma}\left[1 + f'\left(\frac{R_a}{\ell_c}\right)\right]. \tag{14}$$

These adjustments align the mathematical model with physical insights, i.e., rough edges reduce tangential velocity near the boundary through the slip effect (represented by f)[28,29], and enhance the electrostatic driving force through charge concentration (represented by f'). The redistribution of the free charges, in turn, increases the applied torque, potentially causing enhanced rotation in central regions as the charge enhancement dominates over the slip-induced reduction. The above theoretical description is based on the action of surface free charges, therefore, it can be directly applied to frames of different shapes, such as circular and rectangular frames, which are considered in this paper.

Simulation

Considering the geometry of the frames in the experiments and based on the aforementioned theoretical description, we perform systematic simulations for the effects of both roughness of the frame edge and the corner sharpness on the rotational behavior of the embedded liquid thin film. We utilize COMSOL Multiphysics for simulations. Similar to the actual condition, flowing the current through the thin film is supplied by a 30 V constant voltage, and the external electric field of 3.53 kV/m is applied in the perpendicular direction. The thin film is considered to be soap-water (5% soap solution) with an electrical conductivity of $\sigma = 10^{-3}$ S/m and a relative permittivity of 80. Given the circumstances of our experiments, the 2D simulation platform suffices, which not only reduces the computational cost, but also avoids the possible mesh errors arising from the thin film's thickness. The surface charge density is calculated according to Eq. 4, and included in the Navier-Stokes equation, Eq. 2. The boundary conditions are applied in analogy to experimental cases; circular and rectangular smooth frames and their corresponding rough and blunt versions. In the simulations, we also consider different levels of roughness and bluntness to provide a vivid picture of the problem and a comprehensive comparison. The roughness is defined by adding irregularities of random distribution and with a pre-defined standard deviation from the average. The bluntness is defined via changing the sharp corner of a square frame into a circle of varying radius. It is remarkable that for the smooth and rough frames, as explained in Section , we apply no-slip and partial-slip boundary conditions, respectively. The simulation results are presented in terms of the fluid velocity field and multiple extracted associated parameters.

Results and discussion

Inserting a tracer or a set of tracers into a rotating thin film and monitoring their position in time leads to the construction of tracer trajectories and associated velocity fields. Figures 2(a) and 2(b) show the results of a rotating thin film suspended in smooth and rough circular frames, respectively. Similar results for smooth and rough rectangular shape frames are shown in Fig. 2(c) and 2(d), respectively. The actual boundaries of the frames are also shown by dashed lines in all panels. In all four geometries, upon initiation of the motion, an outward migration of particles toward the walls is observed. This radial displacement is indicative of the centrifugal effect arising from the rotational motion of the film. However, this outward migration proceeds only up to a certain limit; as the tracers approach the boundary, their motion stabilizes and continues along nearly steady paths parallel to the wall. This behavior suggests the establishment of a balance between the centrifugal force and the boundary-induced confinement within the film. Supplementary Video 1 presents visually the above behaviors. To validate the theoretical description of the observed phenomena, we present the simulation results in Figs. 2(e) to 2(h), in which identical frames are considered. The trajectories and the reconstructed velocity fields are measured for 2 s in each case to ensure avoiding of over-writing of the simulated values, on the one hand, and to reach a steady state, on the other hand. The colors in the simulation plots show the magnitude of the velocity field. In the circular frame (Fig. 2(a)), the trajectories are smooth and nearly concentric, displaying a high degree of rotational symmetry. The tracers form stable circular orbits that

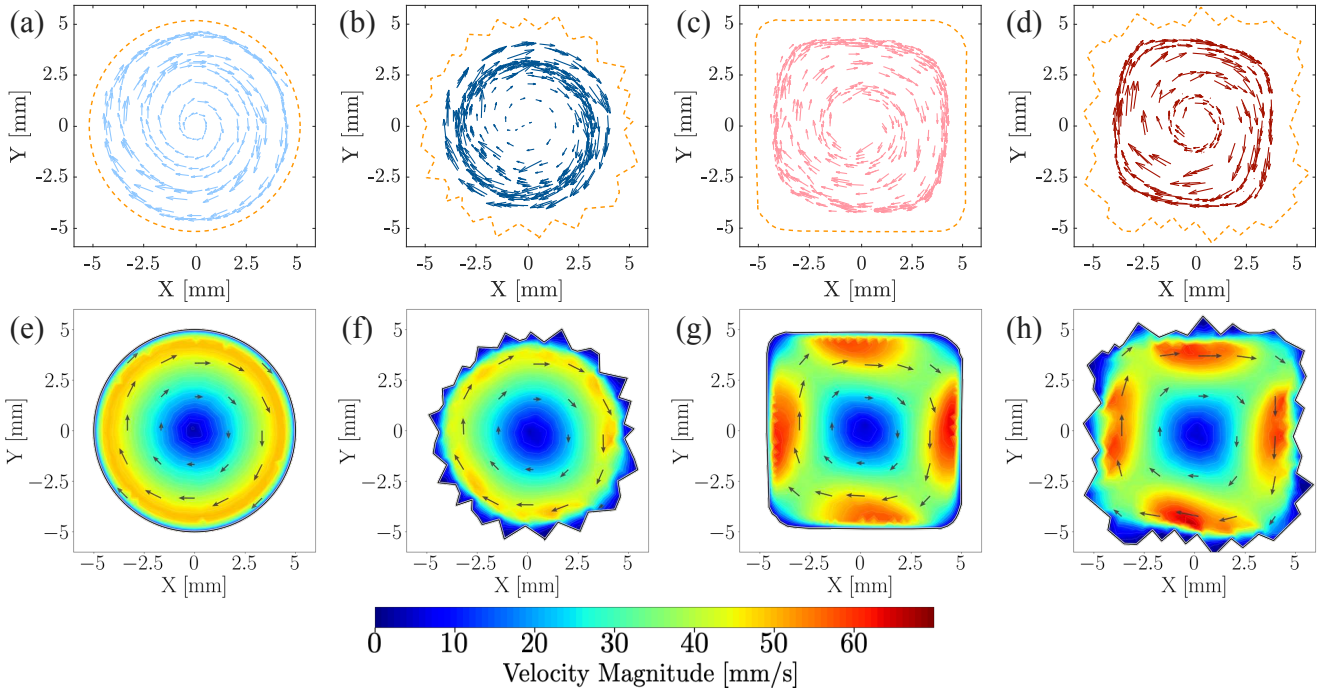


Figure 2. Trajectories of traces and velocity fields of rotating liquid films suspended in four different frame geometries: (a) circular, (b) rough circular, (c) square, and (d) rough square. Solid lines represent the paths of tracers, and dashed lines indicate the corresponding frame boundaries in the XY plane. The simulated velocity fields associated with (e) circular, (f) rough circular, (g) square, and (h) rough square frames are also shown.

remain centered within the film, indicating a uniform flow distribution. When edge irregularities are introduced, as in the rough circular frame (Fig. 2(b)), the general circular pattern persists but with slight distortions near the boundary. These perturbations result from local variations in the edge topography, which modify the boundary conditions and lead to minor deviations in the otherwise symmetric flow. In the rectangular frame (Fig. 2(c)), the tracer paths exhibit a distinct transition; near the film center, the motion remains approximately circular, but as the tracers move outward and sense the boundary, their trajectories gradually deform to follow a square contour. This indicates that the flow field responds to the boundary's geometric constraints, becoming circular in the central region and square-like near the periphery. The rough square frame (Fig. 2(d)) shows a similar overall behavior, though with additional perturbations in the trajectories due to the rough edges. These roughnesses introduce localized distortions near the corners and sides, but the general trend of circular-to-square transition is still observed.

Furthermore, in order to address the bluntness influence in the frame corners, we simulate the velocity field of a frame whose geometry transforms from a square into a circle (Fig. 3). To this end, we define a relative corner curvature $\frac{r_B}{a}$, where r_B is the curvature radius of the corners and a is the size of the square frame side, as shown in the inset of Fig. 3. The simulation results for $\frac{r_B}{a}$=0 (perfect square) to $\frac{r_B}{a}$=0 (perfect circle) in 10 steps are demonstrated. Supplementary video 2 shows smoother variations of the relative curvature. The results demonstrate a critical relative curvature (around $\frac{r_B}{a}$=0.35) after which the boundaries are no longer sensed. The colorbars in Figs. 2 and 3 are defined by assigning the darkest red to the maximum velocity in each figure. In another set of simulation tasks, we apply random roughness with increasing amplitude to the edges of circular and rectangular frames. The results for five levels of roughness are outlined in Figs. 4. The roughness function is examined via considering the Hurst exponent, and for all the progressively applied roughnesses Hurst exponent of 0.1 is taken. However, the amplitude of the roughness, i.e., standard deviation from the mean value, varies from 0 to 0.09. In Figs. 4(a-e), the roughness with amplitude of 0, 0.01, 0.03, 0.06, and 0.09, on the edges of a circular frame are considered, and, in Figs. 4(f-j) similar roughness for a square-shape frame is applied.

The resulted velocity field indicates that the symmetric velocity field is broken, i.e., despite smooth frames, velocities at similar radii vary, and it is more pronounced approaching the edges. In a highly roughened frame, the initial shape of the frame is no longer sensed, which is also observed at the corners of a rectangular frame if compared with the circular one (Figs. 4(a) and 4(f)). Moreover, in the rough frames the velocity field in the central part of the frame follows the overall shape (the envelope curve) of the frame. The maximum local velocity along the radial direction in frames with high roughness is higher, which is consistent with the aforementioned observation that the characteristic parameters of velocity profiles may sense the

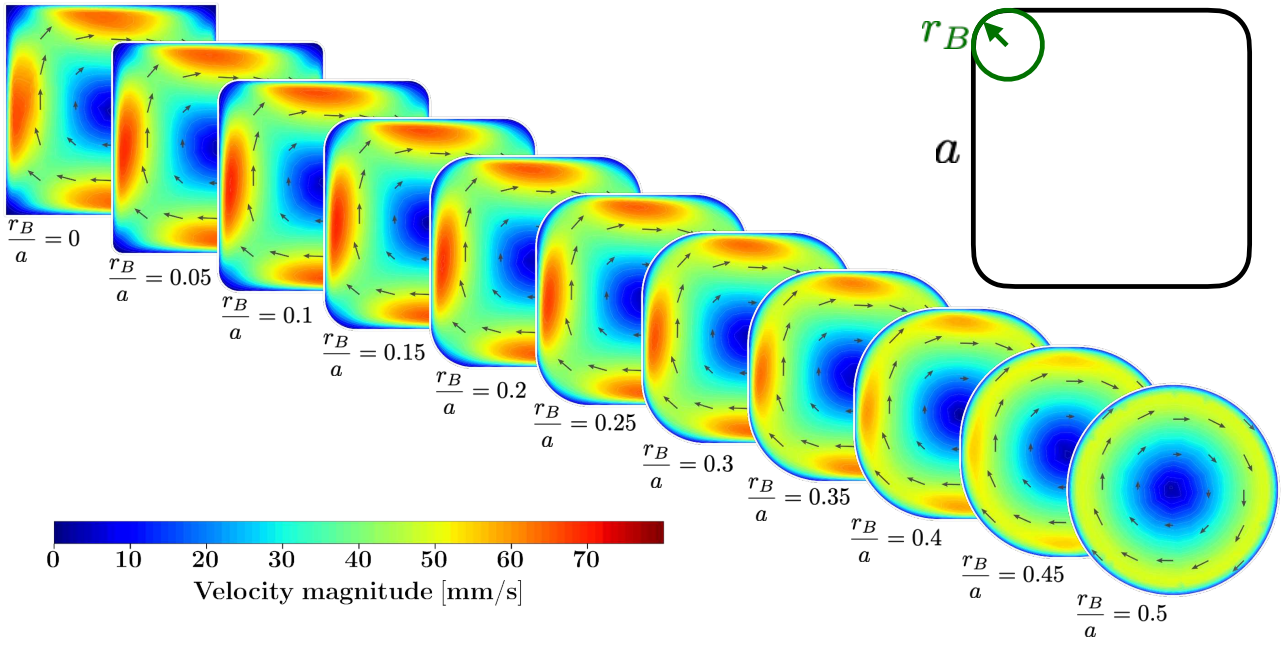


Figure 3. Simulation of the velocity field of a frame whose geometry transforms from a square into a circle, to address the bluntness influence in the frame corners. The inset defines the relative corner curvature $\frac{r_B}{a}$, where r_B is the curvature radius of the corners and a is the size of the square frame side. The simulation results for $\frac{r_B}{a}$=0 (perfect square) to $\frac{r_B}{a}$=0 (perfect circle) in 10 steps are demonstrated. Supplementary Video 2 shows smoother variations of the relative curvature.

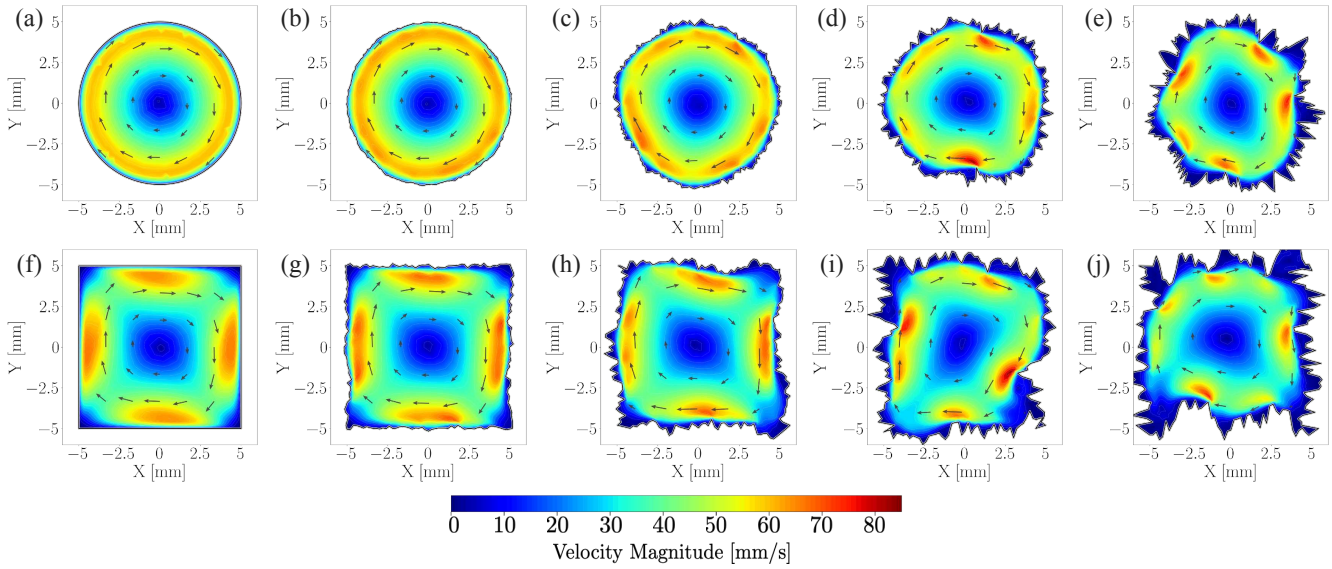


Figure 4. Simulation results for the velocity fields of a (a-e) circular and (f-j) square frames with the roughness with amplitude of 0, 0.01, 0.03, 0.06, and 0.09, on the edges, respectively. For all the progressive applied roughnesses the Hurst exponent of 0.1 is taken.

impact of roughness first for any frame shapes. The shape, expressed in terms of bluntness, is sensed, on the other hand, by the trajectory specifications. The strong gradient of velocity field near the edges can also be deduced from the (almost) stopping fluid flow in the tortuosities of the rough edges.

In order to present the observations in a more quantitative fashion the radial average of velocity profiles of the smooth circular and rectangular frames and their rough versions are plotted. The profile plots and their associated characteristic

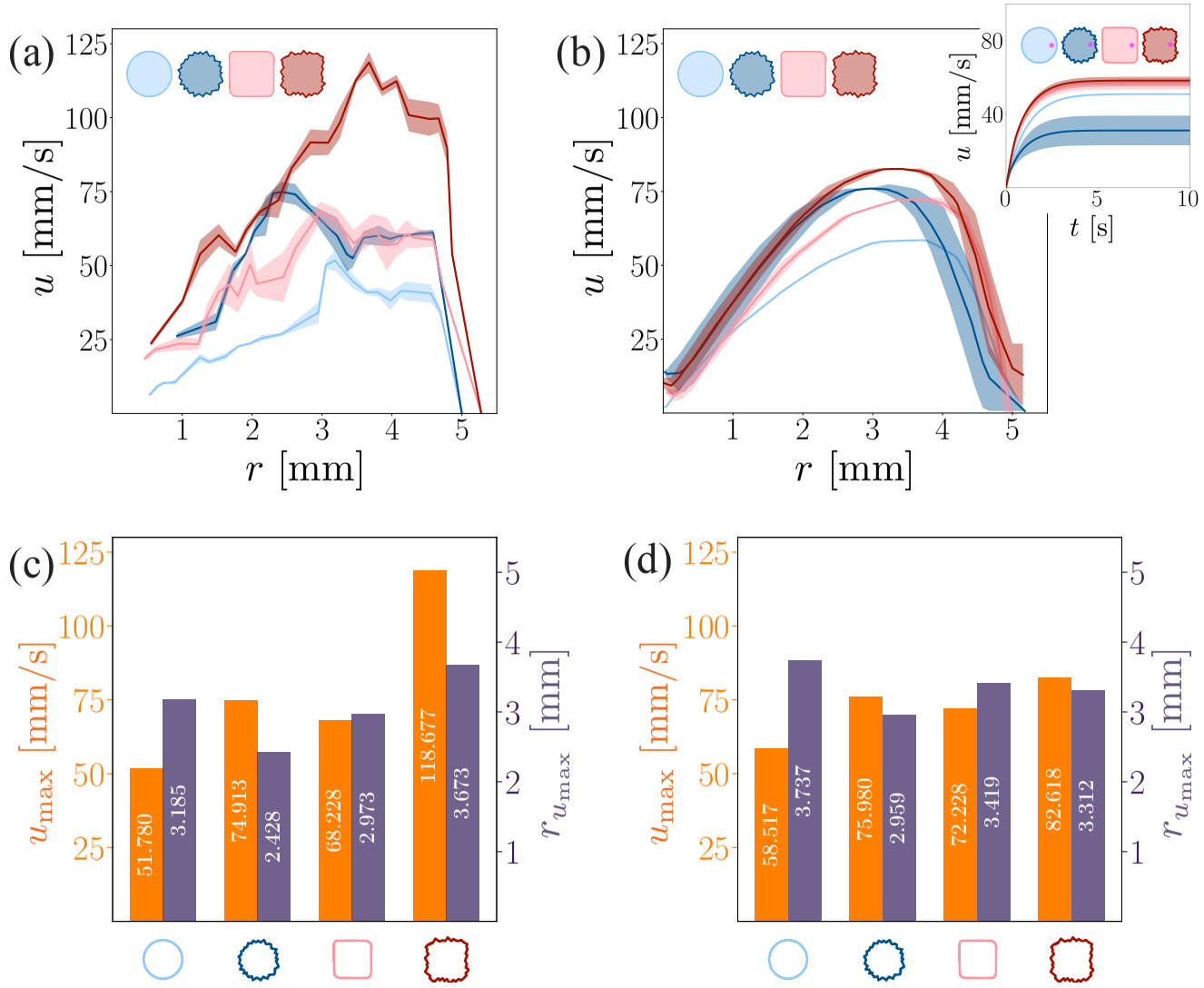


Figure 5. The radial average of velocity profiles of the smooth circular and rectangular frames and their rough versions along radial directions for the (a) experimental and (b) simulation results. The shadow errorbars are for the angular averaging in the profile measurement process. The inset of panel (b) is the velocity of a specific point far away from the center (indicated with a star mark in the legend) over time. The measured values of maxima of velocities ($u_{\max}$) and the radii in which the maxima occur ($r_{u_{\max}}$) for the (a) experimental and (b) simulation results.

parameters are shown in Fig. 5. Figure 5(a) shows the velocity profiles of the four frames obtained from the experimental data on the tracer particle tracking and velocity computing. In Fig. 5(b), similar simulation results are shown. The shadow errorbars are due to the angular averaging in the profile measurement process. Both experiments and simulations demonstrate an increasing velocity as distancing from the center, toward reaching a maximum and a brief plateau, and then a rapid decrease afterwards. The profiles show that the maximum velocity of rectangle frames is higher than that of circular ones, which is in consistence with the results of Fig. 2. The maxima in both frames are higher in rough cases. In the inset of Fig. 5, the velocity of a specific point far away from the center (indicated with a star mark in the legend) in time is plotted, which shows a rapid increase followed by a constant velocity. The measured values of maxima of velocities and the radii in which the maxima occur are shown with bar plots for the experimental data and simulations in Figs. 5(c) and. 5(d), respectively. The experimentally observed trends and the simulations results are in agreement. Overall, these observations demonstrate that the geometry and surface characteristics of the frame play a crucial role in defining the internal flow structure of the liquid film. The circular frame support symmetric and stable rotation, while the square frame imposes geometric modulation on the motion, causing the trajectories to conform progressively to the boundary shape. Edge roughnesses, whether in circular or

square configurations, introduce small local disturbances but do not fundamentally alter the overall flow pattern. These findings highlight the strong coupling between boundary geometry and hydrodynamic behavior in suspended liquid films, providing valuable insights for the design and optimization of liquid film motors. Future studies may explore further modifications to frame shapes and compositions to optimize performance and uncover new phenomena related to fluid dynamics in electrically charged environments.

Conclusion

In conclusion, we have demonstrated that the rotational dynamics of electrically driven thin liquid films are significantly altered by the geometric characteristics of the supporting frame. By systematically investigating the effects of frame shape, edge roughness, and corner sharpness - practical imperfections inherent to fabricated frames - we showed that these structural features play a decisive role in controlling the internal flow behavior of liquid film motors. Our results reveal that circular frames promote symmetric and stable rotational motion, whereas rectangular frames impose geometric modulation on the flow, leading to a progressive transition of fluid streamlines from circular trajectories to paths that conform to the boundary shape. Edge roughness primarily affects the tracer trajectory at early stages, while the overall frame shape predominantly influences the tracer velocity and long-term flow structure. Importantly, although edge roughness and minor surface imperfections introduce local disturbances, they do not fundamentally alter the global rotational pattern of the film. For rectangular frames, our simulations further indicate that the corner curvature relative to the overall frame size governs the transition between circular and boundary-dominated streamlines. These behaviors are consistently explained within the theoretical framework of charge induction in ohmic liquids coupled with hydrodynamic interactions. The demonstrated sensitivity of flow dynamics to geometric constraints suggests promising applications in microfluidic systems for multiple tasks, including mixing, pumping, and separation at the microscale. Future studies may explore a wider range of frame geometries and materials to further optimize rotational performance and uncover new fluidic phenomena.

Data availability

The data that support the findings of this study are available from the corresponding author upon reasonable request.

References

1. Mosadegh, B., Bersano-Begey, T., Park, J. Y., Burns, M. A. & Takayama, S. Next-generation integrated microfluidic circuits. *Lab on a Chip* **11**, 2813–2818 (2011).
2. Agiotis, L. *et al.* Magnetic manipulation of superparamagnetic nanoparticles in a microfluidic system for drug delivery applications. *J. Magn. Magn. Mater.* **401**, 956–964 (2016).
3. Squires, T. M. & Quake, S. R. Microfluidics: Fluid physics at the nanoliter scale. *Rev. modern physics* **77**, 977–1026 (2005).
4. Sonin, A. A. *Freely suspended liquid crystalline films* (Wiley, 2003).
5. Gharib, M. & Derango, P. A liquid film (soap film) tunnel to study two-dimensional laminar and turbulent shear flows. *Phys. D: Nonlinear Phenom.* **37**, 406–416 (1989).
6. Rutgers, M., Wu, X.-l., Bhagavatula, R., Petersen, A. & Goldburg, W. Two-dimensional velocity profiles and laminar boundary layers in flowing soap films. *Phys. Fluids* **8**, 2847–2854 (1996).
7. Najafi, A. & Shirsavar, R. Theoretical explanation of rotational flow in the liquid-film motor. *Sci. Reports* **11**, 23063 (2021).
8. Nasiri, M., Shirsavar, R., Mollaei, S. & Ramos, A. Numerical study of soap-film flow by nonuniform alternating electric fields. *Phys. Rev. E* **95**, 022806 (2017).
9. Amjadi, A., Shirsavar, R., Radja, N. H. & Ejtehadi, M. A liquid film motor. *Microfluid. nanofluidics* **6**, 711–715 (2009).
10. Faetti, S., Fronzoni, L. & Rolla, P. Static and dynamic behavior of the vortex–electrohydrodynamic instability in freely suspended layers of nematic liquid crystals. *The J. chemical physics* **79**, 5054–5062 (1983).
11. De Gennes, P.-G. & Prost, J. *The physics of liquid crystals*. 83 (Oxford university press, 1993).
12. Shirsavar, R., Amjadi, A., Tonddast-Navaei, A. & Ejtehadi, M. Electrically rotating suspended films of polar liquids. *Exp. fluids* **50**, 419–428 (2011).
13. Liu, Z.-Q., Li, Y.-J., Gan, K.-Y., Jiang, S.-R. & Zhang, G.-C. Water film washers and mixers: their rotational modes and electro-hydrodynamical flows induced by square-wave electric fields. *Microfluid. nanofluidics* **14**, 319–328 (2013).

14. Saghaei, T., Moradi, A.-R., Shirsavar, R. & Habibi, M. Liquid bulk rotation induced by electric field at free surface. *Appl. physics letters* **106** (2015).

15. Tsai, P., Daya, Z. A., Deyirmenjian, V. B. & Morris, S. W. Direct numerical simulation of supercritical annular electroconvection. *Phys. Rev. E: Stat. Nonlinear, Soft Matter Phys.* **76**, 026305 (2007).

16. Grosu, F. & Bologa, M. Electroconvective rotation of a dielectric liquid in external electric fields. *Surf. Eng. Appl. Electrochem.* **46**, 43–47 (2010).

17. Liu, Z.-Q., Li, Y.-J., Zhang, G.-C. & Jiang, S.-R. Dynamical mechanism of the liquid film motor. *Phys. Rev. E: Stat. Nonlinear, Soft Matter Phys.* **83**, 026303 (2011).

18. Shirsavar, R. *et al.* Rotation induced by uniform and non-uniform magnetic fields in a conducting fluid carrying an electric current. *RSC advances* **6**, 112641–112645 (2016).

19. Feiz, M., Namin, R. & Amjadi, A. Theory of the liquid film motor. *Phys. Rev. E* **92**, 033002 (2015).

20. Adrian, R. J. *et al.* Particle-imaging techniques for experimental fluid mechanics. *Annu. review fluid mechanics* **23**, 261–304 (1991).

21. Westerweel, J. *Digital particle image velocimetry: Theory and application* (Delft University Press, 1995).

22. Jackson, J. D. *Classical electrodynamics* (John Wiley & Sons, 2021).

23. Amjadi, A., Feiz, M. & Namin, R. M. Liquid soap film generates electricity: a suspended liquid film rotating in an external electric field as an electric generator. *Microfluid. Nanofluidics* **18**, 141–147 (2015).

24. Ponomarev, I. & Meyerovich, A. Surface roughness and effective stick-slip motion. *Phys. Rev. E* **67**, 026302 (2003).

25. Panahi, M. *et al.* 3d monitoring of the surface slippage effect on micro-particle sedimentation by digital holographic microscopy. *Sci. Reports* **11**, 12916 (2021).

26. Niavarani, A. & Priezjev, N. V. The effective slip length and vortex formation in laminar flow over a rough surface. *Phys. Fluids* **21** (2009).

27. Ziarani, A. & Mohamad, A. Effect of wall roughness on the slip of fluid in a microchannel. *Nanoscale microscale thermophysical engineering* **12**, 154–169 (2008).

28. Pan, Y., Jing, D., Zhang, H. & Zhao, X. Effective boundary slip induced by surface roughness and their coupled effect on convective heat transfer of liquid flow. *Entropy* **20**, 334 (2018).

29. Lee, T., Charrault, E. & Neto, C. Interfacial slip on rough, patterned and soft surfaces: A review of experiments and simulations. *Adv. colloid interface science* **210**, 21–38 (2014).

Supplementary information

Acknowledgements

The authors thank to Saeed Mollaei for the helpful discussions and to Mostafa Charmi for providing the electrical equipment.

Competing interests

The authors declare no competing interests.

Funding

No funding was received for this manuscript.

Author contributions

M.P. and M.H.S. conducted the experiments. M.P. analysed the results. M.P. and M.H.S. developed the theoretical model. N.M. helped on the experimental setup and acquisition of data. D.H. worked on the numerical simulations. A.M. conceived and supervised the project. All authors discussed the results and contributed to the writing and reviewing of the manuscript.

Supplementary Files

This is a list of supplementary files associated with this preprint. Click to download.

- SR2026GLFMsupplementary.pdf
- VideoS01mp4.mp4
- VideoS02mp4.mp4